Title: Initiation and mobility of irrigation-induced loess flowslide recurrence on the Heifangtai area in China: Insights from hydrogeological conditions and liquefaction criteria

Authors: Fanyu Zhang [a*], Gonghui Wang [b], Jianbing Peng [c]

(a) MOE Key Laboratory of Mechanics on Disaster and Environment in Western China; Department of Geological Engineering, Lanzhou University, Lanzhou, Gansu Province, 730000, China

(b) Research Center on Landslides, Disaster Prevention Research Institute, Kyoto University, Gokasho, Uji, Kyoto, 611-0011

(c) Department of Geological Engineering, Chang'an University, Xian, Shaanxi Province, 710054, China

Abstract: The Heifangtai area is commonly known as the museum of loess landslides in China. Irrigation-induced loess flowslides frequently recur along the margin cliffs of the Hefaingtai terrace, causing 42 fatalities and significant economic losses, as well as major ecological and environmental problems, such as increased soil erosion rate. The initiation and mobility of these irrigation-induced loess flowslide recurrences remain undetermined. On three typical recurrences of the loess flowslides, we performed joint geophysical detection using electrical resistivity tomography (ERT) and multichannel analysis of surface waves (MASW), and also tested loess basic properties by field profile sampling. In addition, we examined the shear behaviors of saturated

loess utilizing an undrained ring shear apparatus. The geophysical signatures and *in-situ* loess property profiles showed that hydrogeological conditions are key to the initiation of recurring loess flowslides. The results also demonstrated that liquefaction shear behaviors of saturated loess control the mobility of after-failure of the loess flowslides. Rapid criteria of liquefaction susceptibility evaluation are suggested to provide a better understanding of the dynamic mechanisms of loess flowslides. These findings shed substantial light on long-runout flowslides that occur in fine-grain soil and their implications for landslide hazard mitigation.

Keywords: irrigation; loess flowslide; hydrogeological conditions; liquefaction criteria.

1. Introduction

Loess flowslide is among the most common of flow-like landslides, due to the sensitive liquefaction of saturated loess. The 1920 Haiyuan earthquake induced fluidized loess landslides that killed more than 100,000 people (Close and McCormick, 1922; Zhang and Wang, 2007; Huang, 2009). Earthquakes and rainfall, along with irrigation, constitute common triggers of catastrophic loess flowslides in China. With climate change in the Chinese loess plateau, extreme or abnormal rainfall events have begun to more frequently trigger catastrophic loess flowslides. However, irrigation is currently the most common catalyst of this type of fluidized loess landslide, attributable to modern intensive farming.

The Hefangtai area is commonly known as the museum of Chinese loess landslides, and has become a representative of irrigation-induced loess flowslides. It

has attracted significant attention from researchers in different disciplines since the landslide that occurred in the 1980s resulted in lifting the groundwater table. Early literature focused on classification of loess landslides, including loess-bedrock slide, loess flow, loess flowslide, and loess slide (Wu and Wang, 2002). These landslides comprise two movement types of slide and flow, according to the taxonomy suggested by Cruden and Varnes (1996) and Hungr *et al.* (2014). Loess flowslides are the most frequent and catastrophic type in the Hefangtai area due to their rapid speed and long-runout displacement. As a consequence, many scholars investigated the relationship between occurrences of flowslides and mechanical behaviors of saturated loess (Xu *et al.*, 2012b; Zhang *et al.*, 2013; Zhang *et al.*, 2014b; Fan *et al.*, 2017; Qi *et al.*, 2018; Xu *et al.*, 2018; Zhang and Wang, 2018; Liu *et al.*, 2019). These researchers found that liquefaction of the saturated loess is key to the occurrence of loess flowslides. Results from ring shear tests and triaxial tests also showed that saturated loess is a characteristic of typical liquefaction behavior, which present obvious shear softening once failure is initiated, accompanying a rapid increase in pore pressure and a sharp decrease in shear strength (Xu *et al.*, 2012b; Zhang and Wang, 2018; Liu *et al.*, 2019). Numerical modeling results also supported the increase of pore water and decrease of shear strength (Gu *et al.*, 2019; Peng *et al.*, 2019), leading to softening and accumulated deformation of the saturated loess layer underlying the drying loess layer. Considerable research has focused on elucidating the initiation and mobility of flowslides, but much of this work has concerned liquefaction of saturated loess and examining its shear behavior. Indeed, there remains a lack of criteria to

68 evaluate liquefaction susceptibility, which is crucial for a deeper understanding of the
69 dynamic progress of loess flowslides and their hazard evaluation.

70 It is interesting to note that flowslides were found to always recur at the previous
71 crown zone of the pre-landslide (Xu *et al.*, 2012b; Zhang and Wang, 2018). Recently, a
72 great number of monitoring data also showed the seriousness of recurred loess
73 flowslides at a relatively fixed area in the Hefaingtai area (Liu *et al.*, 2018; Xu *et al.*,
74 2020; Zhang *et al.*, 2020). Xu *et al.* (2020) established a real-time and intelligent early
75 warning system, which successfully predicted several loess flowslide recurrences.
76 Nevertheless, there still exists a high risk of current recurrence of loess flowslides in
77 the Heifangtai area (Xu and Yan, 2019). Xu et al. (2012b) reported that the concave
78 topography of the post-landslide scarp is important to flowslide recurrence because it
79 has the potential to raise the groundwater table. However, 43 boreholes and 51 ERT
80 profiles afforded evidence that hydrogeological condition is essential to groundwater
81 table dynamics (Peng *et al.*, 2019) controlling flowslide recurrence in the Hefaingtai
82 area. Although that investigation does not argue for the effect of groundwater on
83 loess flowslide recurrence, precisely how groundwater influences the recurrences
84 remains unclear.

85 In this study, we aim to provide an improved understanding of the initiation and
86 mobility of loess flowslide recurrence in the Hefaingtai area. To achieve this, we
87 performed joint ERT and MASW detections, and field loess property tests, and
88 examined the shear behaviors of saturated loess utilizing an undrained ring shear
89 apparatus. We combined geophysical signatures and *in-situ* loess property profiles to

analyze hydrogeological conditions forming loess flowslide occurrences. In addition, the present study integrates current ring shear test data along with previously published results, as well as loess basic property parameters, to estimate a rapid criteria of liquefaction susceptibility evaluation. Finally, we directly use these findings to elucidate the dynamic mechanisms of loess flowslides, and to address broader issues concerning the mechanics of long-runout flowslides occurring in fine grain soils and their implications for landslide hazard mitigation.

2. Background of the study site

The Heifangtai area is situated on the fourth terrace of the Yellow River, and is a loess platform located 60 km west of Lanzhou City in Gansu Province, China (Fig. 1). The Heifangtai terrace was converted to agricultural land in the 1960s. Due to long-term flooding irrigation, loess flowslides occurred almost annually on the margin cliffs of the terrace, causing 42 fatalities, and serious destruction of buildings and infrastructure, as well as total abandonment of a major national highway along the Yellow River.

We integrated several boreholes, resistivity measurements, and lithological outcrops along the terrace margin. A typical stratigraphic section in descending order can be described as follows: (i) an approximately 20 m thick top layer of Malan loess, essentially comprised of main landslide materials; (ii) a 5-30 m thick layer of Lishi Loess with a discontinuous distribution; (iii) a clay layer of 4-17 m thickness underlying the loess layer, which is key to uplift the groundwater table on the terrace; (iv) a 2-5 m

112 thick layer of alluvial deposits, consisting primarily of well-rounded pebbles sized
113 approximately 5-10 cm in diameter; and (v) a deep layer of undisturbed bedrock
114 comprised of mudstone and sandy mudstone with minor sandstone and conglomerate
115 partings, which is a gentle bedding layer of 180° with a dip of 6-12°, as shown in Fig. 2.
116 The new loess flowslides almost always recurred in the repeated occurrence locations
117 within the scarp of an older one (Fig. 1), which constitutes one of the remarkable
118 features of loess landslides on the Heifangtai terrace.
119

120 **3. Materials and methods**

121 We conducted a field investigation and laboratory measurement, and developed
122 a joint research mode for loess flowslides on the Heifangtai terrace. To do this, we
123 selected three typical zones, i.e., Dangchuan section, Jiaojia section, and Moshigou
124 section (Fig. 1). They all exhibit periodic recurrence of loess flowslides, which
125 represent the features and mechanisms of initiation and mobility of this kind of loess
126 flowslide. To elucidate the hydrogeological conditions controlling and regulating loess
127 flowslide initiation, we performed field profile measurements, 2D electrical resistivity
128 tomography (ERT), and multichannel analysis of surface waves (MASW). To assess the
129 liquefaction behaviors impacting mobility of the loess flowslide, we carried out
130 laboratory basic property measurements and ring shear tests of samples.
131

132 **3.1 Field investigations**

133 We selected the Chenjia loess flowslide (CJF) and the Luojiapo loess flowslide

(LJPF) to perform field profile measurements. The CJF occurred on 29 January 2015 and the LJPF occurred on 29 April 2015. The sampling time is 29 March 2015 and 6 May 2015 for CJF and LJPF, respectively. First, we measured the longitudinal sections after a landslide using a laser range finder (Trupulse 360) with the assistance of a reflective prism. Subsequently, we took undisturbed loess samples on landslide scarps at different depths with a special cutting ring of 5 cm diameter and 10 cm height to measure their water content, natural density, and dry density. We also examined the strength of *in-situ* loess from base to top on the landslide scarps utilizing a penetrometer, and *in-situ* strength was calculated by penetration depth using a correction formula. We also took disturbing loess samples on the landsliding body using a convenient soil sampler. This device is commonly employed in archaeology, and features a semicircular shovelhead and multi-lengthened steel tube. It is capable of obtaining disturbed unsaturated loess up to a depth of 7 m. All of the undisturbed and disturbed loess samples were placed into airtight plastic bags for laboratory basic property measurements.

Concerning the ERT surveys, we used AGI SuperSting R8/IP (Advanced Geosciences, Inc.) to perform 2D resistivity imaging. During the field surveys, we selected Wenner arrays with an electrode spacing of 3 m and 5 m along the desired profile lines (Fig. 1). Electrical profiles were measured using a GPS, and topographic changes were assessed using a laser measuring technique. Finally, we inverted the apparent resistivity data using the newest RES2DINV software. During the inversion, a smoothness-type regularization constrained least-squares was implemented by

156 employing an incomplete Gauss-Newton optimization technique. It is worth noting
157 that we cannot take topographical changes into account along the profiles due to the
158 flat platform with very slight topographic relief. The optimization technique aims to
159 iteratively adjust resistivity to obtain a minimal difference between the calculated and
160 measured apparent resistivity values. The absolute acceptable error provides a
161 measurement of this difference. Usually, when the soil has high water content and low
162 density, there will be low electrical resistivity. Moreover, the electrical resistivity is
163 highly sensitive to water content change in the soil layers. The ERT surveys constitute
164 an effective method to detect hydrogeological features in soil layers and possess a
165 strong capacity to explore their relative deep features.

166 Regarding the MASW surveys, we used McSEIS-SXW (OYO Corp.) and 24
167 geophones with a natural frequency of 4.5 Hz. During the surveys, the geophones
168 were spaced at 2 m intervals along the ERT profile lines (Fig. 1), and a specialized wood
169 hammer approximately 8 kg was utilized as the human seismic source. The sledging
170 points were intermediate between the geophones, and outside of both ends of the
171 survey profile. In general, the MASW can explore a maximum depth of 20 m, and the
172 exploration depth depends on both the intrinsic property of soil layers and the
173 extrinsic seismic source energy. Overall, the softer is the soil layer and the lower is the
174 generated energy, the shallower is the maximum depth reached.

175

176 **3.2 Laboratory measurements**

177 In terms of basic property measurements, we examined field loess samples taken

178 from the landslide scarps and landsliding bodies following the Chinese standards of
179 the Ministry of Construction (GB/T50123, 1999). Their density and water content were
180 measured using the oven-dry method. The wet samples were weighed, and then dried
181 at 105 ℃ for 24 h. Subsequently, the mass of the dry samples was recorded. The dry
182 and natural density, and water content, were calculated. The Atterberg limits of the
183 loess samples were measured by the fall cone joint test, which determines the liquid
184 limit and plastic limit for penetration depths of 17 mm and 2 mm, respectively. The
185 joint test is more convenient to obtain the plastic limit than is the rolling procedure.

186 Concerning liquefied behavior measurements, we performed a series of ring
187 shear tests of saturated loess taken from landslide scarp on the Heifangtai terrace. We
188 utilized the ring shear apparatus at static loading under undrained conditions using
189 torque control mode, which is easier to observe the deformation behavior of the
190 tested saturated samples. The apparatus employed in the present research is the fifth
191 version (DPRI-5), which was developed by the Disaster Prevention Research Institute
192 (DPRI), Kyoto University (Sassa *et al.*, 2004). Detailed information on the design and
193 construction of the undrained ring shear apparatus is given in Wang and Sassa (2002)
194 and Sassa et al. (2003). The DPRI ring shear apparatus offers the advantage of large
195 shear displacement under undrained conditions compared with the triaxial apparatus,
196 which is suitable for making the localized shear behavior reappear on the shear
197 deformation zone. Consequently, the ring shear apparatus has been widely used to
198 examine the residual or steady shear strength of soils for liquefaction assessment and
199 slope stability analysis (Bishop *et al.*, 1971; Bromhead, 1979; Stark and Eid, 1993;

200 Wang and Sassa, 2002; Wang *et al.*, 2007; Stark and Hussain, 2010).

201

202 **4. Results**

203 **4.1 Geophysical signatures from V_s and ERT profiles**

204 Fig. 3 presents the V_s and ERT profiles of the Jiaojia section. The V_s profile clearly
205 shows stratigraphic variability involving a negative relief between 0 and 80 m with low
206 V_s value, although there is only limited exploration depth (Fig. 3a). This is because the
207 Hefaingtai terrace was originally a rough platform, and the low V_s value zones may
208 constitute a filling depression. Meanwhile, the on-site evidence demonstrates that the
209 fluctuation of the underlying bedrock is key to the negative relief. There are also some
210 high V_s value zones at the top surface layer within 3 m depth (Fig. 3a), which are
211 related to local densification ascribed to land subsidence. The two time-lapse ERT
212 profiles expose thicker lithological information with a depth of almost 50 m, and the
213 dry and wet boundary at approximately 26 m depth is revealed by the interface
214 between high and low resistivity (Fig. 3b and c). The boundary location is consistent
215 with the scarp of the CJF, as its left scarp is close to the right starting point of the ERT
216 profile. In addition, there is a lower groundwater table on the first ERT survey than on
217 the second one on the negative relief zone between 0 and 80 m. The changes in
218 resistivity from the two time-lapse ERT profiles clearly show the local top features with
219 high resistivity (Fig. 3d), which is in accordance with the high V_s value zones at the top
220 surface layer.

221 One can see a saddle hump between 70 and 80 m in the ERT profile (Fig. 4a),

222 which corresponds to a small ridge (see Fig. 1b and Fig. 1c). Regarding the dry and wet
223 boundary, the groundwater table decreases gradually from the saddle hump to the
224 starting point (i.e., the right side of the ridge), while its left side shows a slight increase
225 in the groundwater table close to the crown of the MSGF. The right side of the ridge
226 has a small gully with a seasonal spring causing a deep groundwater table due to the
227 release of the spring. Furthermore, the Vs profile reveals a slowly uplifting
228 stratigraphic distribution from the start to the endpoints (Fig. 4b), which also
229 facilitates the release of groundwater at the right side of the ridge.

230 Fig. 5 presents the ERT and V_s profiles at the crown and the left flank of the MSGF
231 on the Moshigou section. In the ERT profile along the road (Fig. 5a), there is a low
232 groundwater table between 0 and 30 m; thereafter, the groundwater table becomes
233 deeper at approximately 18 m depth until a distance of 130 m. One can also see a
234 saddle hump between 105 and 122 m in the ERT profile, which also matches the high
235 V_s value zone (Fig. 5b). Similarly, the site also corresponds to a small ridge, and there
236 is a small gully with a seasonal spring on the right side of the ridge (see Fig. 1b). As a
237 result, the sides of the ridge exhibit two obvious low V_s value zones due to the existing
238 gully. It should be noted that even the deepest groundwater table at approximately
239 18 m is higher compared with the dry and wet boundary of the scarp of the MSGF.
240 This may be associated with groundwater recharge after the MSGF occurred over
241 three years.

242

243 **4.2 Physical-mechanical properties**

Fig. 6 presents the physical-mechanical property profiles of the scarp and landsliding body of the CJF. The sampling time is after three months of the CJF initiation, and thus these samples represent a stable state of the recurring CJF. In its landsliding body (Fig. 6a), the water content of the SD5 and SD4 profiles on the head zone gradually increase until approximately 4 m depth, and then remain constant at approximately 25%. Moreover, in the SD4 profile, the water content of the upper 1 m of the loess layer exceed 20%, and low water content loess is markedly thin compared with the SD5 profile. This is because the SD5 profile is very close to the scarp of the CJF, and the low water content of loess derives from incompletely disintegrated dry loess of the scarp (Fig. 6c). Nevertheless, SD3 and SD2 profiles on the travel zone have a combined high-water content of approximately 20% in the loess deposited layer, and the lack of deeper data of the SD2 is due to loess liquefaction resultant from the sampling disturbance. The SD1 profile close to the landslide toe also has a relative high-water content of approximately 20% above 2.5 m, and then it slightly decreases. This slight decrease in water content of deeper loess may be related to the pore water pressure dissipation of the loess. It is worth noting that the high-water content of the loess layer is greater on the landslide head zone than on the travel zone and the landslide toe zones (Fig. 6a), which is attributed to long-term groundwater recharge from the CJF landslide scarp. Fig. 6b shows the physical-mechanical property profiles of the landslide scarp of the CJF. An obvious boundary can be seen at 26 m depth. Above this boundary, the loess layer exhibits a dry state with a water content of approximately 10% and a natural density of approximately 1.5 g/cm^3, as well as high

strength with continuous decrease with increasing depth. Below the boundary, the water content of the loess layer is increasingly closed due to the saturated condition, and its natural density and strength remain almost constant and show an obvious decrease. The data reveal that a softened loess layer under the dry loess layer exists in the scarp of the CJF.

Fig. 7 presents the physical-mechanical property profiles of the scarp and landsliding body of the DJCF. All of the samplings were immediately finished after 7 d of DJCF occurrence when the security restrictions were lifted. Therefore, these properties reflect the recurrence conditions of the DJCF. The water content profiles of the DJCF exhibit changes that differ from those of the CJF, as shown in Fig. 6a. The SD5 profile adjacent to the scarp of the DJCF has high water content, except for the surface loess layer within 0.5 m, and the whole SD4 profile has high water content. These findings are associated with the release of groundwater after the DJCF occurrence. The SD4 and SD 3 profiles have a short sampling depth due to the loess liquefaction. The SD2 profile has relatively low water content on the red clay layer, and the SD1 profile first exhibits an increase in water content, and then the water content decreases and increases again. These changes could contribute to the multiple mobilized covers due to the multiple failures of the LJPF. The scarp of the DJCF presents an almost similar change in physical-mechanical property from top to end in the profile to that of the CJF (Figs. 6b and 6c). A typical boundary can also be discerned between dry and wet loess layers. However, there is a slight difference in strength and density, which may be related to the lack of wetting front above the boundary

ascribed to the rapid sampling. This means that the LJPF initiation releases groundwater reserved in the loess terrace, and its restoration may require a duration of several months, as in the case of the CJF.

Overall, the CJF and LJPL have almost similar physical-mechanical properties on their scarp, in which the same boundary exists between wet loess and dry loess. The softened zone under the dry loess layer is key to the initiation of loess flowslides on the Heifangtai terrace. There is also a difference in water content profiles on the landsliding body of the CJF and LJPL. This difference is especially prominent in the saturated loess deposited on the landsliding body, which is important to maintain its long-runout mobility.

4.3 Typical shear liquefaction behaviors

The typical shear liquefaction behaviors of the saturated loess are presented in Figs. 8 and 9. We only show the results of two saturated loess at the void ratio of 0.751 and 0.744, as Zhang and colleagues have published several groups of ring shear test results of saturated loess from the Heifangtai terrace (Zhang *et al.*, 2013; Zhang *et al.*, 2014a; Zhang and Wang, 2018). Figs. 8a and 9a plot normal stress, shear resistance, and pore pressure against shear displacement, Figs. 8b and 9b present an effective stress path, and Figs. 8c and 9c illustrate the time series data of sample height (i.e., vertical displacement) and shear displacement. In Figs. 8a and 9a, to facilitate a clearer view of the generation of pore pressure accompanying shear displacement in the initial shearing period, a logarithmic abscissa of shear displacement within the range

of 0.1 m was taken; thereafter, a linear abscissa was used to show that the test had been sheared to a steady-state (point SSP). Some pore-water pressure was built-up with shear deformation before the peak shear strength (point F); whereas, after the onset of failure, pore-water pressure exhibited a marked increase, and shear strength experience a rapid reduction. This period is usually known as the collapse period, largely due to the failure of the meta-stable structure (Wang and Sassa, 2002). After this, pore-water pressure, shear resistance, and vertical sample height gradually tended to become constant, accompanying a further increase in shear displacement at steady-state shear strength (point SSP). In the two tests, the effective stress path tended leftward with increasing shear stress, and finally reached their respective peak shear strength (point F); thereafter, the path descended towards its steady-state strength (point SSP). There was a very slight increase in shear resistance, which is attributed to the little contraction of the loose sample, as shown in Figs. 8c and 9c. No similar increase in shear resistance was found when the saturated loess had stronger densification or cementation (Zhang *et al.*, 2013; Zhang *et al.*, 2014b; Zhang and Wang, 2018). Theoretically, there should be no volume change in undrained shear of the saturated sample, but it is inevitable due to the slight contraction during the shear zone development prior to failure. It is interesting to note that this progress matches the pore water pressure built by shear deformation. Furthermore, greater vertical and shear deformations will occur on the loose sample than on the compacted sample with longer deformation time. This finding is in accordance with that obtained in preliminary ring tests (Zhang and Wang, 2018).

5. Discussion

5.1 Hydrogeological conditions of loess flowslide initiation

Geophysical signatures and loess property measurements provide useful information on hydrogeological conditions. The Heifangtai terrace is a nearly flat platform, but its underlying stratum is rugged under loess layers. The geophysical signatures in the present research confirmed this fact (Figs.3~5), which was also supported by previous ERT surveys (Peng *et al.*, 2019). The underlying stratigraphic relief is key to the difference in the spatial distribution of perched groundwater. This is because it controls the spatial distribution of loess landslides and its differences in movement types (Xu *et al.*, 2014; Peng *et al.*, 2019). Meanwhile, the perched groundwater is easier to converge into the negative relief zone of the underlying rugged stratum (Figs. 3~5). The *in-situ* water content profiles revealed that the scarp of recurring loess flowslide exhibits a shallower groundwater table than its two flanks (Qi *et al.*, 2018). The numerical simulation demonstrates that the groundwater table is higher on the concave topography of the scarp of a recurring loess flowslide than that of its lateral slopes (Xu *et al.*, 2012b). In addition, the simulation results show that the groundwater table rises faster at recurring loess flowslide sites than at other zones under irrigation conditions on the Heifangtai terrace (Xu *et al.*, 2012b). This finding is consistent with observations of time-lapse ERT profiles in the Jiaojia section (Fig. 3), and measurements of the groundwater table in the Dangchuan section (Peng *et al.*, 2019). Consequently, we explain why the recurring loess flowslides initiated always at

post-landslide sites as follows. The negative relief of the underlying stratum becomes an important path of the groundwater, which is fundamental to accumulate the groundwater and uplift its table. Moreover, its rapid recovery of the groundwater table at post-landslide sites also contributes to the recurrence of loess flowslides in the Heifangtai terrace.

It is well known that irrigation water infiltration plays a critical role in the groundwater regime in the Heifangtai terrace (Zhou, 2012; Zhang *et al.*, 2013; Zhou *et al.*, 2014; Zeng *et al.*, 2016). The recharge and variation of groundwater regulate initiation of the recurring loess flowslides, which depend on the boundary between dry and wet loess (Figs. 6 and 7). Usually, irrigation water infiltrates to underlying the low-permeable layers along cracks in overlying loess, causing recharge of the groundwater and its table uplift (Xu *et al.*, 2012a; Zhou *et al.*, 2014; Zeng *et al.*, 2016; Pan *et al.*, 2019). Therefore, the wet loess layer becomes thicker, and the softened zone sustains a thinner dry loess layer, while its strength is diminished (Figs. 6 and 7). The load of the overlying loess layer holds persistently on the weakly softened zone, producing unremitting shear deformation with very slight vertical deformation prior to abrupt failure (Figs. 8c and 9c). It is interesting to note that the deformation behavior from the ring shear tests is highly similar to the displacement curves of these recurring loess flowslides, as observed by Xu *et al.* (2020). This supports the speculation that excess pore pressure builds up before initiation, and liquefaction is a consequence of shear failure, as shown in Figs 8 and 9. As a result, the initiation of the loess flowslides recurs at the pre-landslide sites, which has been proven by multiple

recurrence events, such as the LJPL, on the Heifangtai terrace.

Furthermore, the groundwater uplift induced recurrence of the MSGL, and the uplift is related to water pipe leakage on the crown of the MSGL. A similar event of loess flowslide occurred in loess agricultural irrigation of Shanxi Province resultant from water leakage from the canal (Zhang *et al.*, 2009). Meanwhile, it is worth noting that the CJF initiated in the low groundwater table, as shown in Fig. 3b. Previous studies found that there was a rapid loss of lateral support provided by the water when the groundwater table decreased (Zhou *et al.*, 2014), and this was accompanied by an observed decrease in shear strength of saturated loess with a salt leaching process (Zhang *et al.*, 2013; Zhang *et al.*, 2014b; Fan *et al.*, 2017; Qi *et al.*, 2018). Therefore, this could be attributed to the joint effects of hydrodynamic pressure and pore water chemistry on initiation of the CJL under the low groundwater condition.

5.2 Liquefaction criteria to loess flowslide mobility

5.2.1 Liquefaction susceptibility

To evaluate liquefaction susceptibility fine-grained soil is crucial to analyze the probability of flow-like mobility after landslide initiation because it provides a basic criterion to preliminarily assess the liquefaction potential of the soil. Some authors made detailed reviews and developed suggestions for liquefaction susceptibility criteria (Seed, 1987; Andrews and Martin, 2000; Boulanger and Idriss, 2004; Boulanger and Idriss, 2006; Bray and Sancio, 2006; Juang *et al.*, 2006; Moss *et al.*, 2006). Among these suggestions, rapid liquefaction susceptibility assessment is commonly used, and

based on soil index properties and *in-situ* penetration tests. The penetration tests, commonly applied through the standard penetration test (SPT) and the piezo-cone penetration test (CPTU), could provide first-hand geotechnical information about a site. In addition, over time, the index property methods have become increasingly convenient and cost-effective. Bray and Sancio (2006) developed a criterion for fine-grained soils based on a plastic index and ratio of water content to liquid limit. Indeed, previous study also revealed that the criterion is a useful method to rapidly assess the liquefaction susceptibility of loess and its mobility at different water content (Zhang *et al.*, 2019).

Utilizing the criterion developed by Bray and Sancio (2006), we assess the liquefaction susceptibility of the loess samples from the scarp of the CJF and LJPF (Fig. 10a). All samples at saturation water content are in the susceptible zone to liquefaction, which is in accordance with the liquefied behavior of saturated or near saturated loess in the landsliding body (Figs. 6 and 7). The results show that the loess in the Heifangtai terrace is easily liquified when its water content is close to the liquid limit. As shown in the plasticity chart (Fig. 10b), a very slight variation exists in the plastic and liquid limits of the loess, which is because the nature of the loess is relatively constant in the same site. Based on the liquefaction susceptibility criterion advanced by Bray and Sancio (2006), in addition to water content data from the landsliding body of the CJF and LJPF (Figs. 6 and 7), these mobilized materials of the two loess flowslides have almost liquefied during movement. Meanwhile, Seed *et al.* (2003) used the plasticity chart to propose another liquefaction susceptibility criterion,

wherein the fine soils with plastic index ≤ 12 and liquid limit ≤ 37, as well as water content > 0.8*LL, are considered potentially susceptible to liquefaction. According to Seed *et al.'s* criterion, the loess of the Heifangtai terrace is also susceptible to liquefaction, as shown in Fig. 10b. *In-situ* flow-like features confirm the validity of the above two liquefaction susceptibility criteria, which support qualitative analysis of the mobility of the landslides. The Chinese Loess Plateau is covered by sandy, silty, and clayey loess (Liu, 1985), but there is no markedly great variability in the nature of loess, such as minerals and grain sizes, and corresponding small changes in Atterberg limits. Here, we examine the boundary of Atterberg limits suggested by Seed *et al.* (2003), and suggest an adjusted plasticity chart as a rapid and simple method to pre-assess the liquefaction susceptibility of the Chinese loess, as shown in Fig. 10b, wherein there are three zones: susceptible, not susceptible, and further studies are required to determine liquefaction. Along with Bray and Sancio's criterion, our proposed method facilitates a quick judgment of liquefaction susceptibility of different loess.

5.2.3 Pore pressure ratio

Liquefaction failure on a slope results in flow-like landslides with rapid long-runout mobility, which usually includes pore pressure generation and shear resistance decrease. As a consequence, the saturated loess in the present research is a typical characteristic of liquefaction failure, i.e., it undergoes obvious loss of shear resistance and generation of pore pressure during large unidirectional undrained shear deformation, as shown in Figs 8 and 9. Previous researches from the Heifangtai terrace

reported that the saturated loess could generate high pore pressure during shear deformation (Zhang *et al.*, 2013; Zhang *et al.*, 2014b). Some scholars also determined that pore pressure generation controls fluidization of loess flowslides triggered by the 1920 Haiyuan earthquake (Zhang and Wang, 2007; Wang *et al.*, 2014). Visibly, the high pore pressure is closely related to the initiation of liquefaction of the loess and the mobility of loess flowslides on the Heifangtai terrace.

Seed (1987) pointed out that pore pressure build-up is vital to liquefaction of soil, and thus suggested the pore pressure ratio as an index to assess initiation of liquefaction of soil. If the pore pressure ratio does not exceed approximately 0.6, its liquefaction will not occur in the soil, as suggested by Seed (1987). Fig. 11 presents the relation of pore pressure ratio versus void ratio. The figure also includes published data from the Heifangtai terrace concerning saturated loess at different salt concentrations and void ratios (Zhang *et al.*, 2013; Zhang *et al.*, 2014b; Zhang and Wang, 2018), along with four datasets from other loess areas in China (Zhang and Wang, 2007; Wang *et al.*, 2014). The results demonstrate that all of the saturated loess liquefied, and almost all of their pore pressure ratios exceeded 0.6. Furthermore, even though there are two dense samples with a void ratio of approximately 0.68, their pore pressure ratio remains very close to the critical level of 0.6 (Fig. 11). This shows that all saturated loess generates high pore pressure, thus causing consequent liquefaction. Therefore, the pore pressure ratio of approximately 0.6 could constitute a reasonable criterion to evaluate liquefaction initiation of Chinese loess.

464 **5.2.3 Steady-state line**

465 Liquefaction susceptibility could also be evaluated by undrained steady-state
466 shear strength, at which the soil mass flows continuously at constant stress, constant
467 volume, and constant deformation rate (Poulos, 1981). This is essentially a procedure
468 of stability analysis, in which driving shear stress is higher than undrained steady-state
469 shear strength. As Poulos *et al.* (1985) indicated, the undrained steady-state shear
470 strength has a unique function regarding the void ratio of the soil. This constitutes the
471 so-called steady-state line, which is the same as the well-known critical state line (Yang,
472 2002). Generally, liquefaction occurs only in contractive soils above the steady-state
473 line; whereas, dilative soils are not susceptible to liquefaction below the steady-state
474 line (Poulos *et al.*, 1985).

475 Fig. 12 presents the steady-state lines of Chinese loess. In the figure, we utilize
476 undrained ring shear test data from the Heifangtai terrace, published ring shear data
477 from the Xiji area (Zhang and Wang, 2007; Wang *et al.*, 2014), and unpublished ring
478 shear data from the Lanzhou and Mingxian areas. A good logarithmic relationship is
479 found between the steady-state strength and the void ratio of the saturated loess. As
480 a result, the present steady-state line is specific to the Chinese Loess Plateau, because
481 the data involve an extensive area with different loess. The steady-state lines of the
482 loess present the same trend as that of sand (Wang and Sassa, 2002). However, loess
483 possesses a different mechanism from that of sands. For dense sand, provisionally
484 shear dilative behavior exists at the limited defamation, and pore pressure generation
485 contributes primarily to grain crushing with large shear deformation post-failure

(Wang and Sassa, 2002). In contrast, loess generally exhibits fully shear contractive behavior during the entire shearing process with large displacement (Zhang *et al.*, 2013; Zhang *et al.*, 2014b), even in relatively dense loess specimens (Zhang and Wang, 2018). However, the previous investigations demonstrated that shear dilative behavior also takes place in saturated loess in triaxial tests (Zhang *et al.*, 2017; Zhang *et al.*, 2019). Consequently, we compare the difference in the steady-state line constructed by triaxial shear test data (Yang *et al.*, 2004; Zhou *et al.*, 2010; Jiang *et al.*, 2014), as a dark red line shown in Fig. 12. Although triaxial shear data have the same good logarithmic regression line as that in ring shear data, a striking difference in shear resistance is evident when the void ratio is greater than 0.85 for all of the presented data. This difference can be ascribed to two key factors. One is that the triaxial shear apparatus has very limited shear deformation, leading to incomplete shear failure in relatively dense loess specimens, i.e., they do not achieve a real steady state. The previous ring shear test results from relatively dense loess specimens support this assertion, because these dense specimens require greater deformation and a longer time prior to the initiation of failure, and restrain pore pressure generation after the initiation of failure (Zhang and Wang, 2018). Meanwhile, Wang and Sassa (2002) showed that undrained steady-state strength is difficult to reach in triaxial shear tests, especially for medium or dense sand specimens. The second key factor is that the triaxial shear apparatus could make the deformation reappear in the localized shear zone, where the localized shear zone develops within the specimens (Finno *et al.*, 1996). For this reason, the steady-state line derived from ring shear test data should

508 have superior applicability to liquefaction evaluation of Chinese loess, irrespective of
509 whether these soils are in a loose or dense state.
510
511 **5.4 Implications for loess flowslides**
512 First, we suggested a basic framework for liquefaction susceptibility evaluation of
513 Chinese loess, based on the perspective of the dependence of nature, state, and
514 behavior of soil on each other. In this framework, we integrate composited and
515 granular characteristics, water content and void ratio, and shear strength behavior to
516 evaluate the liquefaction susceptibility of loess. This constitutes a substantial
517 advancement over merely building upon available liquefaction evaluation procedures.
518 It is also highly useful to mitigate the frequent occurrence of loess flowslide hazards
519 in the Chinese Loess Plateau. Additional data are still requisite, of course, to improve
520 the suggested framework, because Chinese loess exhibits spatiotemporal differences
521 of its various properties.
522 Second, we prepared two datasets of undrained steady-state shear strength and
523 pore pressure ratio. They are two important parameters to evaluate liquefaction
524 susceptibility, according to the criterion suggested by Seed (1987) and the procedure
525 provided by Poulos *et al.* (1985), respectively. In addition, the two datasets are highly
526 beneficial to analyze the mobilized progress of flow-like landslides in numerical models.
527 They also constitute two key input parameters in popular simulation methods, for
528 example, the DAN model (Hungr and McDougall, 2009), the Massflow model (Ouyang
529 *et al.*, 2015), and LS-RAPID (Sassa et al., 2010). Generally, these models empirically

select constant shear strength and pore pressure ratio during numerical simulation based on certain experimental data. Nevertheless, the undrained steady-state shear strength and pore pressure ratio are not only state-dependent, but also water chemical environment-dependent. Furthermore, previous study revealed that a small change in pore pressure ratio determines whether or not a landslide could produce rapid movement (Sassa et al., 2010). As consequence, reasonable selection of the steady-state strength and pore pressure ratio are crucial to accurately simulate dynamic progress of flow-like landslides in hazard mitigation and risk assessment.

6. Conclusions

The results of the current study lead to the following three main conclusions:

(1) The joint geophysical surveys can increase certainty of detected hydrogeological conditions by comparing their signatures and combining *in-situ* evidence. The geophysical signatures from Vs and ERT profiles, along with the *in-situ* loess property profiles, demonstrated that the negative relief zone of the underlying rugged stratum more easily converges groundwater, forming the perched water layer. As a result, recurred loess flowslides are generally initiated in negative relief zones under the Heifangtai terrace.

(2) The *in-situ* physical-mechanical properties and laboratory ring shear results demonstrated that the saturated loess is highly susceptible to liquefaction. The increase in pore pressure accumulates slightly during deformation prior to liquefaction initiation, and it transitions to rapid augmentation when liquefaction

552 occurs. The liquefaction of saturated loess is the result of loess flowslide initiation and,
553 consequently, long run-out mobility with common high speed, rather than the cause
554 of shear failure.
555 (3) The suggested liquefaction criteria are based on the nature and state of loess,
556 which could rapidly evaluate liquefaction susceptibility using Atterberg limits, pore
557 pressure ratio, and steady-state strength of loess. The datasets of pore pressure ratio
558 and steady-state strength are also useful to analyze mobilized progress of loess
559 flowslides for their hazard evaluation.
560 **Declaration of Competing Interest:** The authors declare that they have no known
561 competing financial interests or personal relationships that could have appeared to
562 influence the work reported in this paper.
563
564 **Knowledges:** This study was supported by the National Natural Science Foundation of
565 China (No. 41977212 and 41927806). The first author thanks their help of Dr. Guan
566 Chen, Dr. Yi Zhang, and Runqiang Zeng at Lanzhou University in the field of ERT
567 detection.
568

569 **References**

570 Andrews, D.C.A., Martin, G.R., 2000. Criteria for liquefaction of silty soils. Proceedings of the 12th World
571 Conf. on Earthquake Engineering, Upper Hutt, New Zealand, NZ Soc. for EQ Engrg., Paper No. 0312.
572 Bishop, A.W., Green, G.E., Garga, V.K., Andresen, A., Brown, J.D., 1971. A new ring shear apparatus and
573 its application to the measurement of residual strength. Géotechnique 21, 273-328.
574 Boulanger, R., Idriss, I., 2006. Liquefaction susceptibility criteria for silts and clays. Journal of
575 Geotechnical and Geoenvironmental Engineering 132, 1413-1426.
576 Boulanger, R.W., Idriss, I.M., 2004. Evaluating the potential for liquefaction or cyclic failure of silts and
577 clays. Rep. UCD/CGM-04/ 01, Univ. of Calif., Davis, Calif.

Bray, J.D., Sancio, R.B., 2006. Assessment of the liquefaction susceptibility of fine-grained soils. Journal of Geotechnical and Geoenvironmental Engineering 132, 1165-1177.
Bromhead, E.N., 1979. A simple ring shear apparatus. Ground Engineering 12, 40-44.
Close, U., McCormick, E., 1922. Where the mountains walked. National Geographic Magazine 41, 445-464.
Cruden, D.M., Varnes, D.J., 1996. Landslides: investigation and mitigation. Chapter 3-Landslide types and processes. Transportation research board special report.
Fan, X., Xu, Q., Scaringi, G., Li, S., Peng, D., 2017. A chemo-mechanical insight into the failure mechanism of frequently occurred landslides in the Loess Plateau, Gansu Province, China. Engineering Geology 228, 337-345.
Finno, R.J., Harris, W.W., Mooney, M.A., Viggiani, G., 1996. Strain localization and undrained steady state of sand. Journal of Geotechnical and Geoenvironmental Engineering 122, 462-473.
GB/T50123, 1999. Standard for soil test method. Ministry of Construction, P.R. China, (in Chinese).
Gu, T., Zhang, M., Wang, J., Wang, C., Xu, Y., Wang, X., 2019. The effect of irrigation on slope stability in the Heifangtai Platform, Gansu Province, China. Engineering Geology 248, 346-356.
Huang, R., 2009. Some catastrophic landslides since the twentieth century in the southwest of China. Landslides 6, 69-81.
Hungr, O., Leroueil, S., Picarelli, L., 2014. The Varnes classification of landslide types, an update. Landslides 11, 167-194.
Hungr, O., McDougall, S., 2009. Two numerical models for landslide dynamic analysis. Computers & Geosciences 35, 978-992.
Jiang, M., Zhang, F., Hu, H., Cui, Y., Peng, J., 2014. Structural characterization of natural loess and remolded loess under triaxial tests. Engineering Geology 181, 249-260.
Juang, C., Fang, S., Khor, E., 2006. First-order reliability method for probabilistic liquefaction triggering analysis using CPT. Journal of Geotechnical and Geoenvironmental Engineering 132, 337-350.
Liu, F., Xu, Q., Zhang, Y., Frost, J.D., Zhang, X., 2019. State-dependent flow instability of a silty loess. Géotechnique Letters 9, 22-27.
Liu, T., 1985. Loess and Environment. Science Press, Beijing, (in Chinese).
Liu, X., Zhao, C., Zhang, Q., Peng, J., Zhu, W., Lu, Z., 2018. Multi-temporal loess landslide inventory mapping with C-, X- and L-band Sar datasets—A case study of Heifangtai loess landslides, China. Remote Sensing 10, 1756.
Moss, R., Seed, R., Kayen, R., Stewart, J., Der Kiureghian, A., Cetin, K., 2006. CPT-Based Probabilistic and Deterministic Assessment of In Situ Seismic Soil Liquefaction Potential. Journal of Geotechnical and Geoenvironmental Engineering 132, 1032-1051.
Ouyang, C., He, S., Tang, C., 2015. Numerical analysis of dynamics of debris flow over erodible beds in Wenchuan earthquake-induced area. Engineering Geology 194, 62-72.
Pan, P., Shang, Y.-q., Lü, Q., Yu, Y., 2019. Periodic recurrence and scale-expansion mechanism of loess landslides caused by groundwater seepage and erosion. Bulletin of Engineering Geology and the Environment 78, 1143-1155.
Peng, D., Xu, Q., Zhang, X., Xing, H., Zhang, S., Kang, K., Qi, X., Ju, Y., Zhao, K., 2019. Hydrological response of loess slopes with reference to widespread landslide events in the Heifangtai terrace, NW China. Journal of Asian Earth Sciences 171, 259-276.
Poulos, S.J., 1981. The steady state of deformation. Journal of the Geotechnical Engineering Division, ASCE 107, 553-562.

622 Poulos, S.J., Castro, G., France, J.W., 1985. Liquefaction evaluation procedure. Journal of geotechnical
623 engineering 111, 772-792.
624 Qi, X., Xu, Q., Liu, F., 2018. Analysis of retrogressive loess flowslides in Heifangtai, China. Engineering
625 Geology 236, 119-128.
626 Sassa, K., Fukuoka, H., Wang, G., Ishikawa, N., 2004. Undrained dynamic-loading ring-shear apparatus
627 and its application to landslide dynamics. Landslides 1, 7-19.
628 Sassa, K., Nagai, O., Solidum, R., Yamazaki, Y., Ohta, H., 2010. An integrated model simulating the
629 initiation and motion of earthquake and rain induced rapid landslides and its application to the 2006
630 Leyte landslide. Landslides 7, 219-236.
631 Seed, H.B., 1987. Design problems in soil liquefaction. Journal of geotechnical engineering 113, 827-845.
632 Seed, R., Cetin, K., Moss, R., Kammerer, A., Wu, J., Pestana, J., Riemer, M., Sancio, R., Bray, J., Kayen, R.,
633 2003. Recent advances in soil liquefaction engineering: A unified and consistent framework.
634 Centercollege of Engineering, University of California, Berkeley.
635 Stark, T.D., Eid, H.T., 1993. Modified Bromhead Ring Shear Apparatus Geotechnical Testing Journal 16,
636 100-107.
637 Stark, T.D., Hussain, M., 2010. Shear Strength in Preexisting Landslides. Journal of Geotechnical and
638 Geoenvironmental Engineering 136, 957-962.
639 Wang, G., Sassa, K., 2002. Post-failure mobility of saturated sands in undrained load-controlled ring
640 shear tests. Canadian Geotechnical Journal 39, 821-837.
641 Wang, G., Sassa, K., Fukuoka, H., Tada, T., 2007. Experimental study on the shearing behavior of
642 saturated silty soils based on ring-shear tests. Journal of Geotechnical and Geoenvironmental
643 Engineering 133, 319-333.
644 Wang, G., Zhang, D., Furuya, G., Yang, J., 2014. Pore-pressure generation and fluidization in a loess
645 landslide triggered by the 1920 Haiyuan earthquake, China: A case study. Engineering Geology 174, 36-
646 45.
647 Wu, W., Wang, N., 2002. Basic types and active features of loess landslide. The Chinese Journal of
648 Geological Hazard and Control 13, 36-40.
649 Xu, L., Coop, M.R., Zhang, M., Wang, G., 2018. The mechanics of a saturated silty loess and implications
650 for landslides. Engineering Geology 236, 29-42.
651 Xu, L., Dai, F., Tu, X., Tham, L., Zhou, Y., Iqbal, J., 2014. Landslides in a loess platform, North-West China.
652 Landslides 11, 993-1005.
653 Xu, L., Dai, F.C., Tham, L.G., Zhou, Y.F., Wu, C.X., 2012a. Investigating landslide-related cracks along the
654 edge of two loess platforms in northwest China. Earth Surface Processes and Landforms 37, 1023-1033.
655 Xu, L., Qiao, X., Wu, C., Iqbal, J., Dai, F., 2012b. Causes of landslide recurrence in a loess platform with
656 respect to hydrological processes. Natural Hazards 64, 1657-1670.
657 Xu, L., Yan, D., 2019. The groundwater responses to loess flowslides in the Heifangtai platform. Bulletin
658 of Engineering Geology and the Environment.
659 Xu, Q., Peng, D., Zhang, S., Zhu, X., He, C., Qi, X., Zhao, K., Xiu, D., Ju, N., 2020. Successful
660 implementations of a real-time and intelligent early warning system for loess landslides on the
661 Heifangtai terrace, China. Engineering Geology 278, 105817.
662 Yang, J., 2002. Non-uniqueness of flow liquefaction line for loose sand. Géotechnique 52, 757-760.
663 Yang, Z., Zhao Chenggang, Wang Lanmin, Rao Weiguo, 2004. Liquefaction behaviors and steady state
664 strength of saturated loess. Chinese Journal of Rock Mechanics and Engineering 23, 3853-3860 (in
665 Chinese).

Zeng, R.Q., Meng, X.M., Zhang, F.Y., Wang, S.Y., Cui, Z.J., Zhang, M.S., Zhang, Y., Chen, G., 2016. Characterizing hydrological processes on loess slopes using electrical resistivity tomography – A case study of the Heifangtai Terrace, Northwest China. Journal of Hydrology 541, Part B, 742-753.

Zhang, D., Wang, G., 2007. Study of the 1920 Haiyuan earthquake-induced landslides in loess (China). Engineering Geology 94, 76-88.

Zhang, D., Wang, G., Luo, C., Chen, J., Zhou, Y., 2009. A rapid loess flowslide triggered by irrigation in China. Landslides 6, 55-60.

Zhang, F., Kang, C., Chan, D., Zhang, X., Pei, X., Peng, J., 2017. A study of a flowslide with significant entrainment in loess areas in China. Earth Surface Processes and Landforms 42, 2295-2305.

Zhang, F., Pei, X., Chen, W., Liu, G., Liang, S., 2014a. Spatial variation in geotechnical properties and topographic attributes on the different types of shallow landslides in a loess catchment, China. European Journal of Environmental and Civil Engineering 18, 470-488.

Zhang, F., Wang, G., 2018. Effect of irrigation-induced densification on the post-failure behavior of loess flowslides occurring on the Heifangtai area, Gansu, China. Engineering Geology 236, 111-118.

Zhang, F., Wang, G., Kamai, T., Chen, W., 2014b. Effect of pore-water chemistry on undrained shear behaviour of saturated loess. Quarterly Journal of Engineering Geology and Hydrogeology 47, 201-210.

Zhang, F., Wang, G., Kamai, T., Chen, W., Zhang, D., Yang, J., 2013. Undrained shear behavior of loess saturated with different concentrations of sodium chloride solution. Engineering Geology 155, 69-79.

Zhang, F., Yan, B., Feng, X., Lan, H., Kang, C., Lin, X., Zhu, X., Ma, W., 2019. A rapid loess mudflow triggered by the check dam failure in a bulldoze mountain area, Lanzhou, China. Landslides 16, 1981-1992.

Zhang, Y., Meng, X.M., Dijkstra, T.A., Jordan, C.J., Chen, G., Zeng, R.Q., Novellino, A., 2020. Forecasting the magnitude of potential landslides based on InSAR techniques. Remote Sensing of Environment 241, 111738.

Zhou, Y., 2012. Study on landslides in loess slope due to infiltration. University of Hong Kong.

Zhou, Y., Zhang, D., Luo, C., Chen, J., 2010. Experimental research on steady strength of saturated loess. Rock and Soil Mechanics 31, 1486-1496 (in Chinese).

Zhou, Y.F., Tham, L.G., Yan, R.W.M., Xu, L., 2014. The mechanism of soil failures along cracks subjected to water infiltration. Computers and Geotechnics 55, 330-341.

Figure captions

Fig. 1. (a) Location of the study site; (b) landslide inventory of the Heifangtai terrace; and (c)~(e) typical recurring sites on the Heifangtai terrace.

Fig. 2. Lithological profile of the Heifangtai area.

Fig. 3. V_s and ERT profiles on the Jiaojia section. (a) MASW survey; (b) and (c) ERT surveys; and (d) changes in electrical resistivity.

Fig. 4. ERT and V_s profiles on the right flank and the crown of the MSGF on the Moshigou section. (a) ERT survey; and (b) MASW survey.

Fig. 5. ERT and V_s profiles at the crown and the left flank of the MSGF on the Moshigou section. (a) ERT survey; and (b) MASW survey.

Fig. 6. Physical-mechanical property profiles of the scarp and landsliding body of the CJF. (a) Profiles of water content at different sampling holes of the landsliding body; (b) profiles of water content, density, and strength of the landslide scarp; and (c) sampling profile on the scarp and feature of the landslide head.

Fig. 7. Physical-mechanical property profiles of the scarp and landsliding body of the LJPF. (a) Profiles of water content at different sampling holes of the landsliding body; (b) profiles of water content, density, and strength of the landslide scarp; and (c) sampling profile on the scarp and feature of the landslide head.

Fig. 8. Undrained ring shear test on sample saturated loess at a void ratio of 0.751. (a) Shear resistance versus shear displacement; (b) effective stress path; and (c) vertical sample height and shear displacement resistance versus elapsed time.

Fig. 9. Undrained ring shear test on sample saturated loess at a void ratio of 0.744. (a)

718 Shear resistance versus shear displacement; (b) effective stress path; and (c) vertical
719 sample height and shear displacement resistance versus elapsed time.
720 **Fig. 10.** Liquefaction susceptibility evaluation of loess samples from the scarp of the
721 CJF and LJPF. (a) Criterion developed by Bray and Sancio (2006); and (b) modified
722 plasticity chart as a rapid and simple method to pre-assess liquefaction susceptibility
723 of the Chinese loess.
724 **Fig. 11.** Pore pressure ratio versus void ratio of saturated loess at different areas.
725 **Fig. 12.** Steady-state line of saturated loess at different areas from ring shear test data
726 (black color) and triaxial shear test data (dark red color).
727

728 Fig. 1

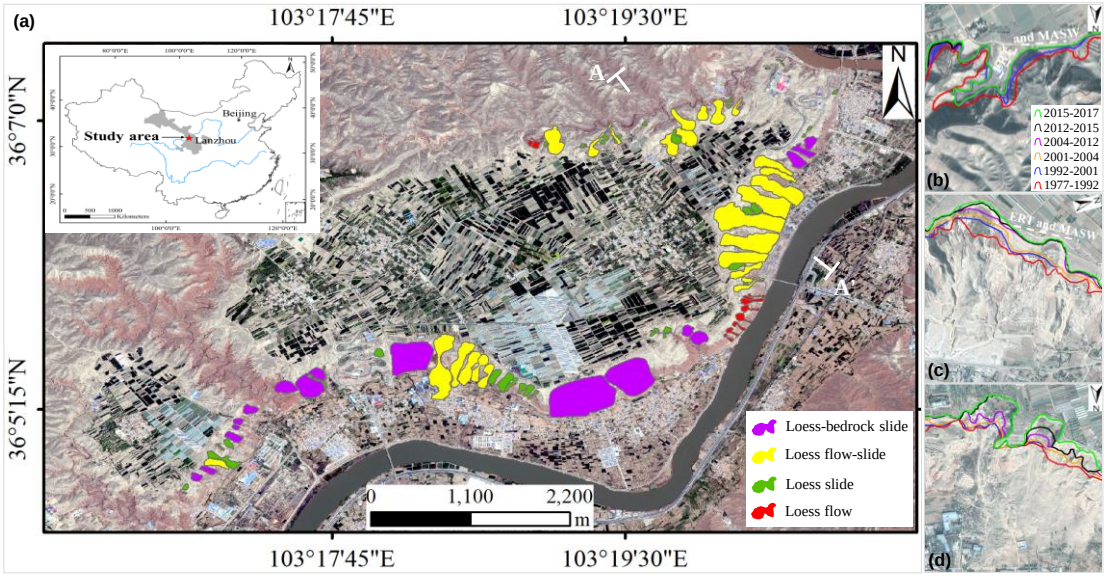

729

730

731 Fig. 2

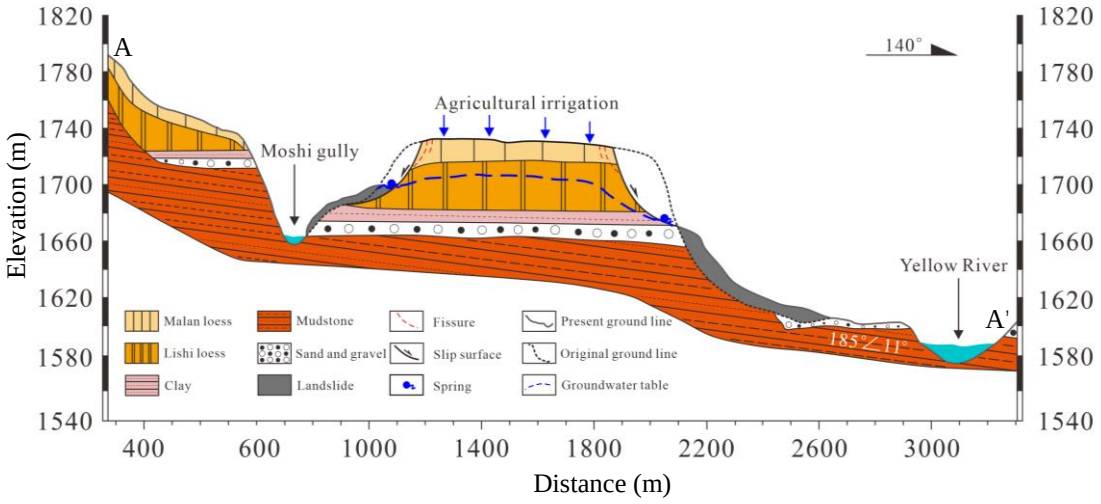

732

733

734 Fig. 3

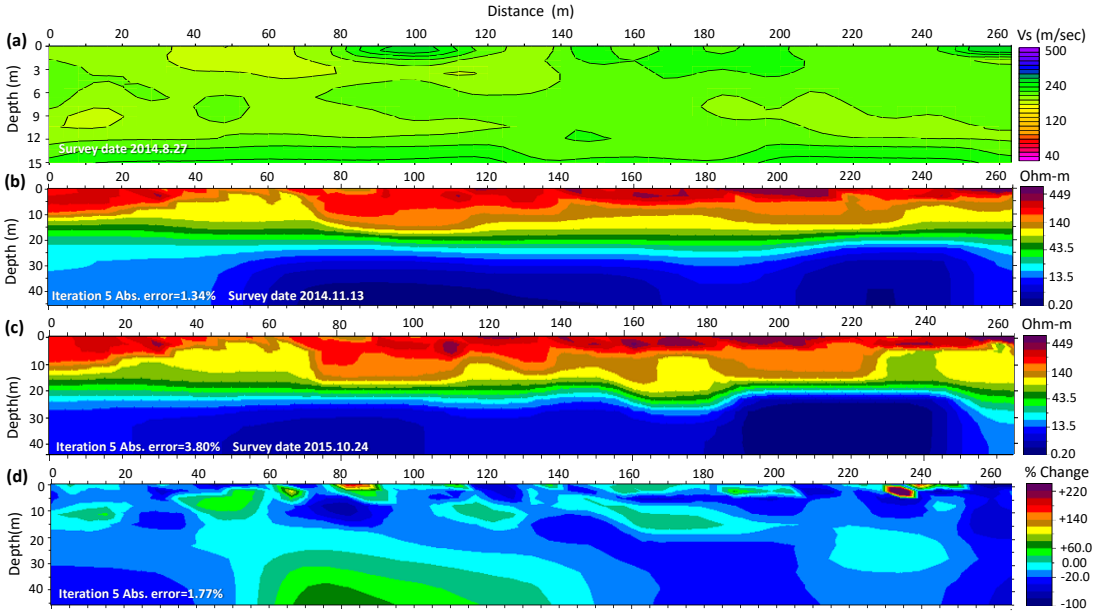

735

736

737 Fig. 4

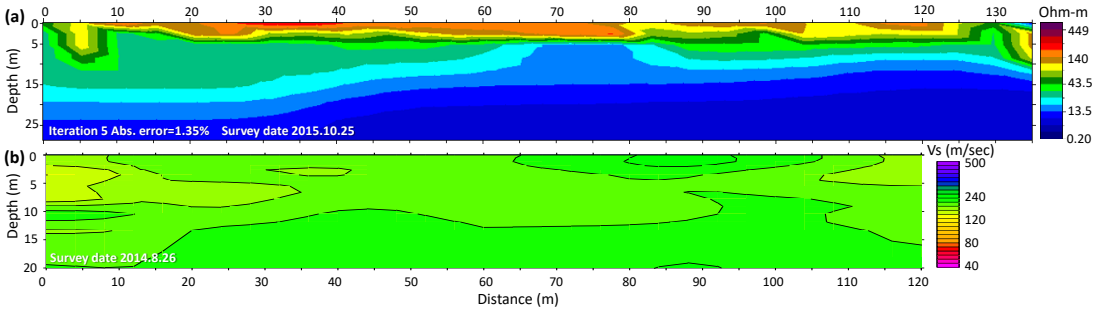

738

739

740 Fig. 5

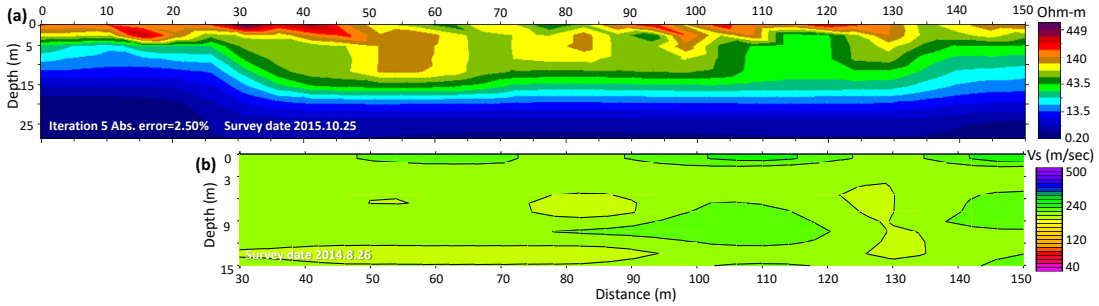

741

742

743 Fig. 6

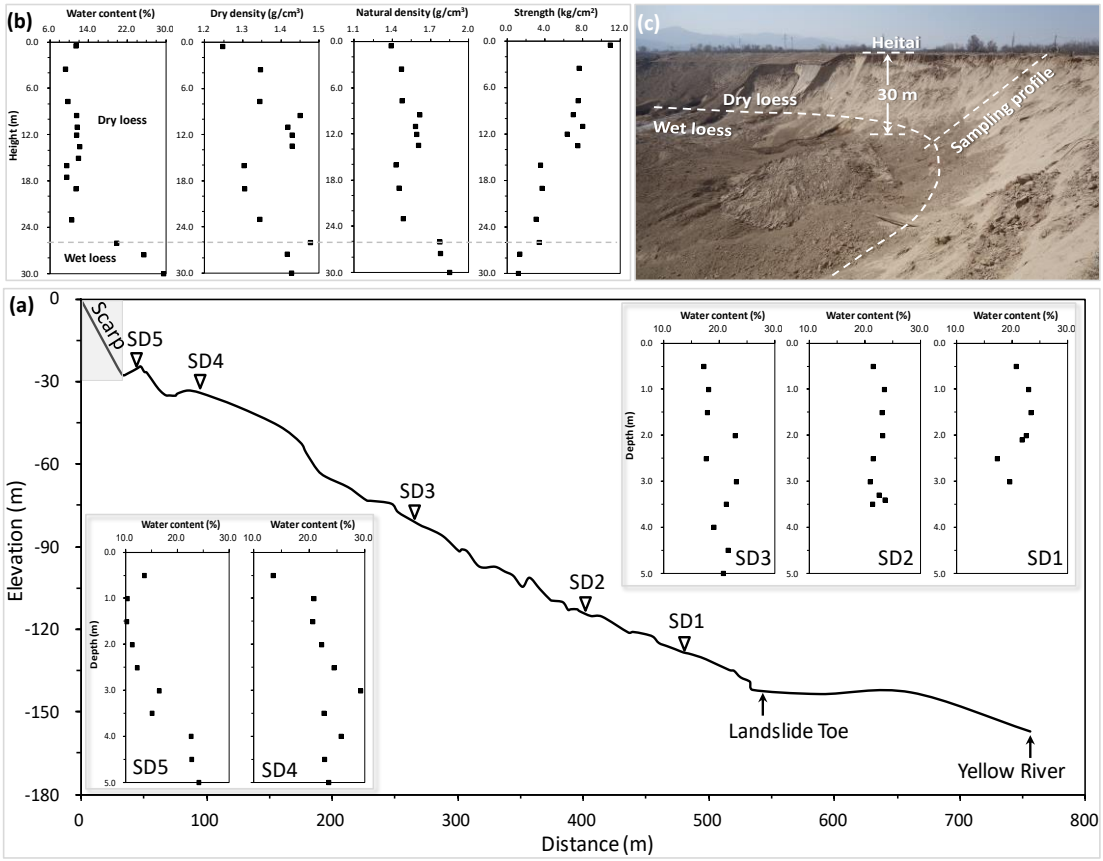

744

745

746 Fig. 7

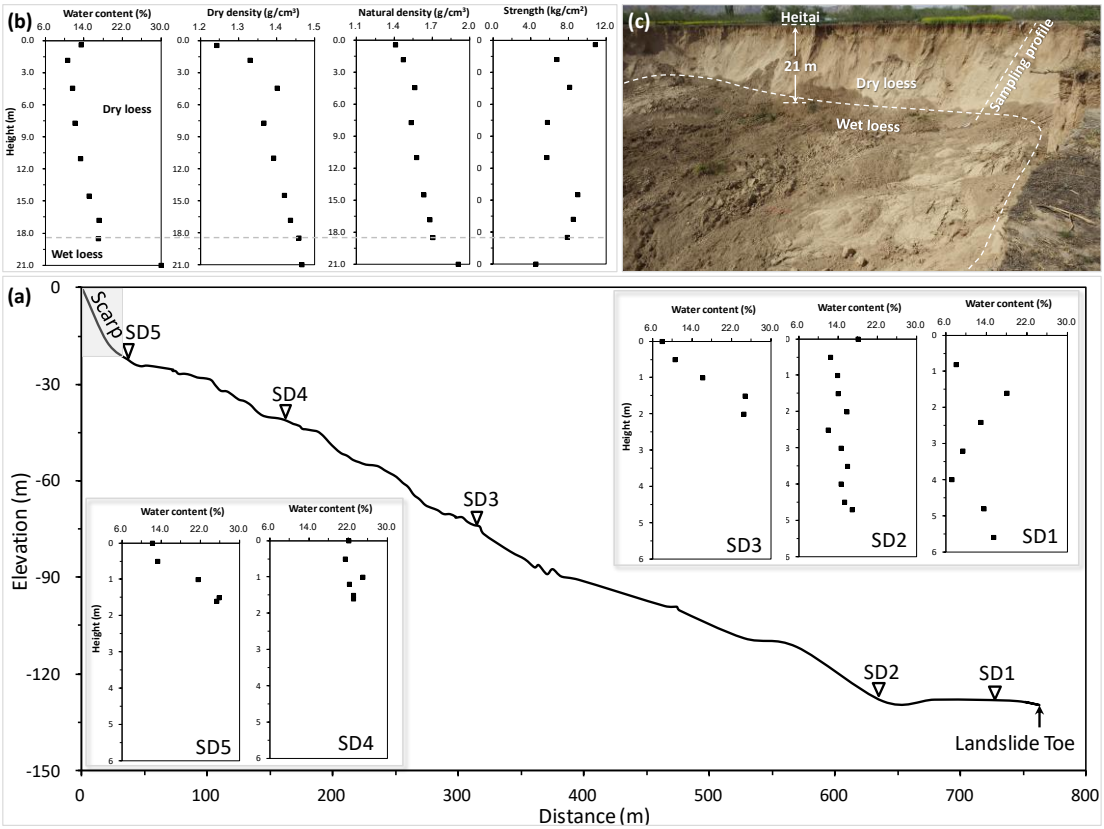

747

748

749 Fig. 8

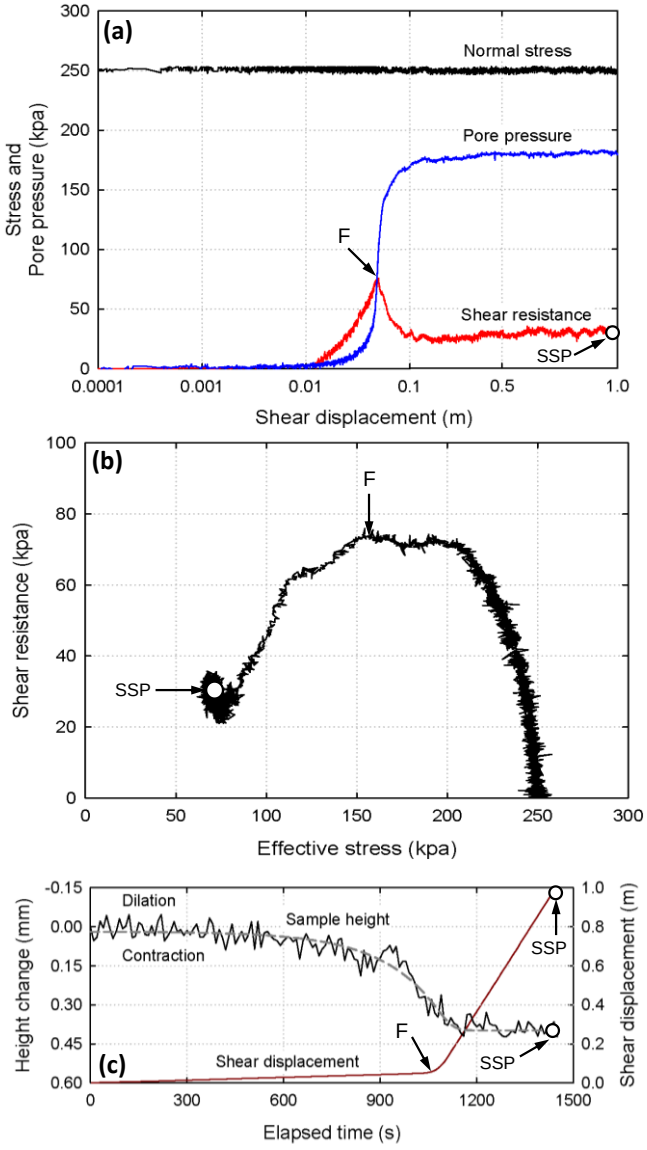

750

751

752 Fig. 9

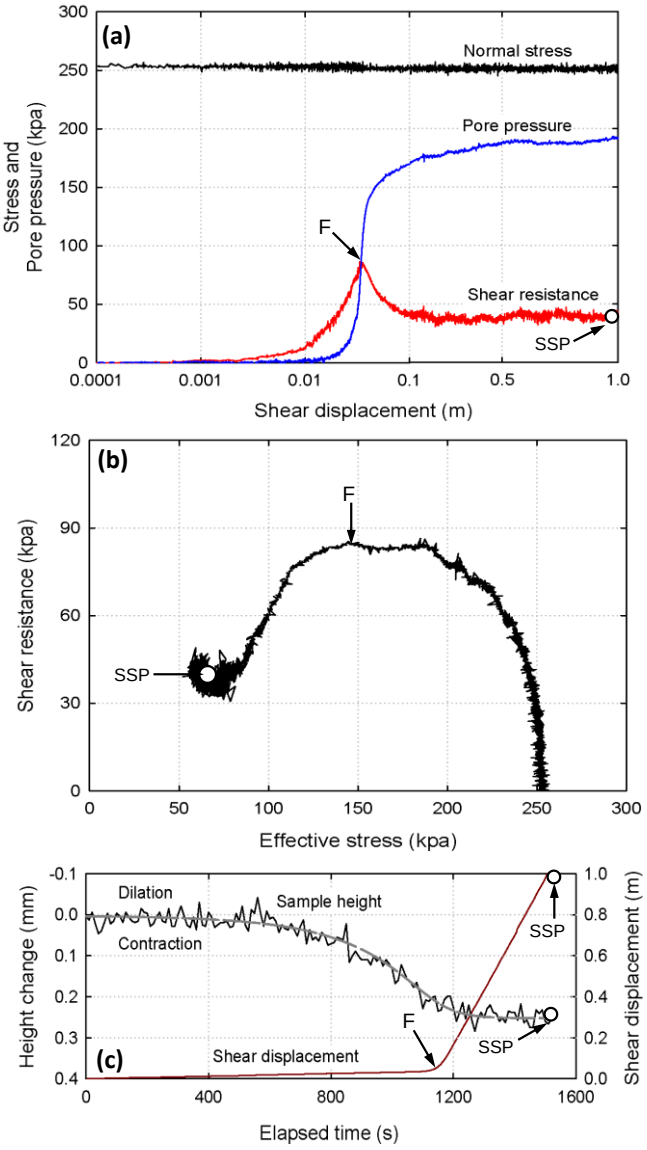

753

754

755 Fig. 10

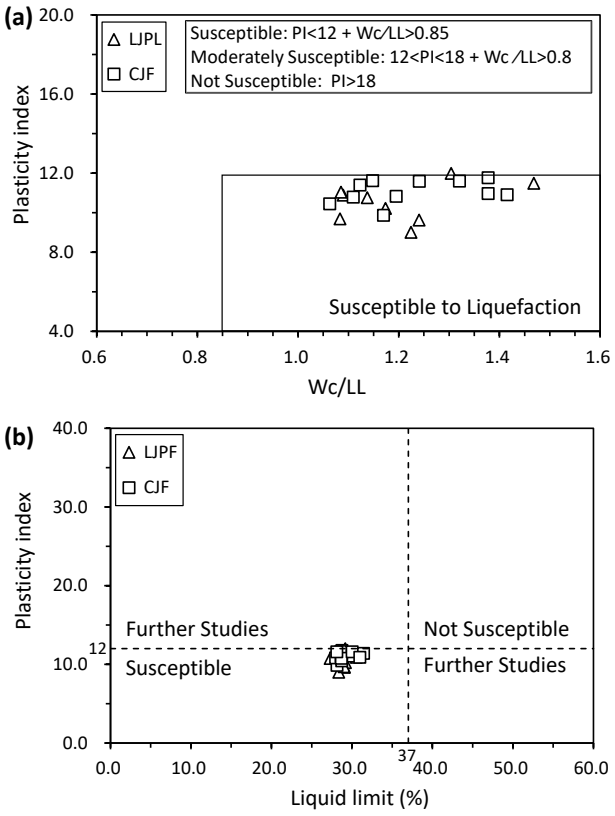

756

757

758

759 Fig. 11

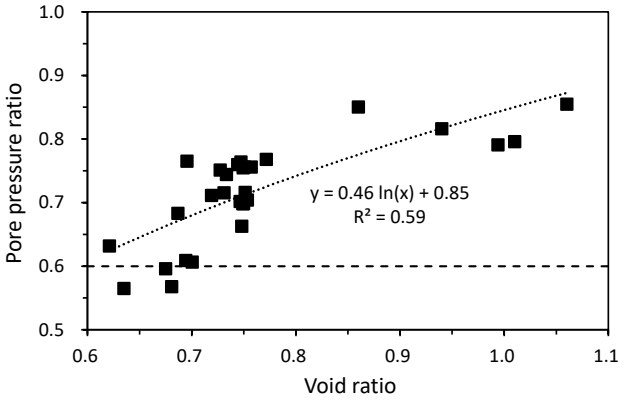

760

761

762 Fig. 12

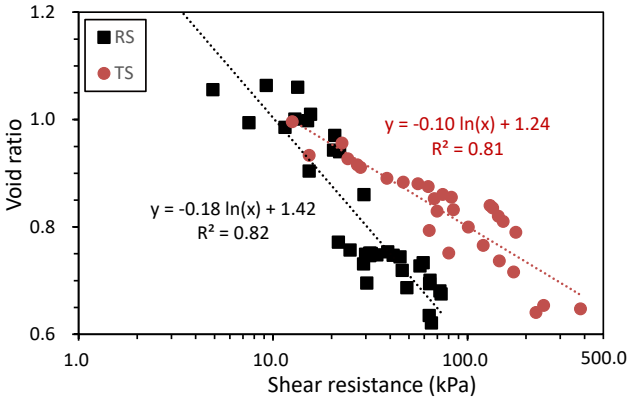

763